Materials Transactions, Vol. 61, No. 4 (2020) pp. 750 to 757

Molecular Dynamics Simulation of Nucleation from Undercooled Melt of Nickel–Aluminum Alloy and Discussion on Polymorphism in Nucleation

Shunsuke Orihara[1], Yasushi Shibuta[1,*] and Tetsuo Mohri[2]

[1]*Department of Materials Engineering, The University of Tokyo, Tokyo 113-8656, Japan*
[2]*Institute for Materials Research, Tohoku University, Sendai 980-8577, Japan*

Nucleation from undercooled melt of Ni–Al alloy is investigated by molecular dynamics (MD) simulation. Multiple nucleation of NiAl nuclei with B2 structure appears from undercooled melt of Ni–50 at%Al, which forms a fine microstructure of B2-NiAl. On the other hand, stepwise phase transition happens from undercooled melt of pure Ni, which is known as Ostwald's step rule. That is, body-centered-cubic (BCC) phase appears first from the undercooled melt and then face-centered-cubic (FCC) nucleation occurs from the inside of previously existing BCC nucleus. Origin of the polymorphism in stepwise nucleation of Ni and the preferential nucleation of B2-NiAl from melt of Ni–Al alloy is discussed on the basis of classical nucleation theory. [doi:10.2320/matertrans.MT-M2019353]

(Received December 2, 2019; Accepted January 6, 2020; Published February 7, 2020)

Keywords: *molecular dynamics simulation, nucleation, polymorphism, nickel–aluminum alloy, intermetallic compound*

1. Introduction

Nucleation is a fundamental phenomenon of a first-order phase transition and it appears on every scene of pattern formation process.[1)] In association with materials science and metallurgy, nucleation is essential for producing practical products of metallic materials since most of metallic materials are produced via nucleation and solidification.[2)] Therefore, it is essential to understand a nature of nucleation from both fundamental and practical viewpoints. However, it is not straightforward to capture a kinetic picture of nucleation since it is difficult to observe nucleation directly during production process of practical materials. Meanwhile, molecular dynamics (MD) simulations have contributed to shed light on a kinetic picture of nucleation[3)] such as nucleation rate,[4,5)] polymorph,[6,7)] non-classic behavior[8,9)] and athermal nucleation.[10)] Moreover, multiple nucleation in recent large-scale MD simulations with more than billion atoms enabled direct formation of polycrystalline microstructure via nucleation,[11,12)] which drastically pushed up the role of MD simulations in the field of computational metallurgy.[13,14)] For more information, MD studies on nucleation in past few decades are closely reviewed by Sosso and coworkers.[3)]

However, MD studies on nucleation of alloy system are not so many at present compared to those of pure metals whereas most of practical products of metallic materials consist of alloys and compounds. This is mainly due to the lack of established potentials for alloys system in the past. Fortunately, recent progress in the development of interatomic potentials for many practical alloys including intermetallic compounds[15–17)] encourages us to push forward MD simulations of nucleation for various alloy systems such as Ni–Pd,[18)] Ni–Ti,[19)] Al–Cu,[20)] Ni–Al,[21)] Cu–Zr,[21)] Ni–Zr[22)] and Ni–Al–Pt.[23)] However, there are few studies of contentious processes of nucleation, solidification and microstructure formation of intermetallic compounds although some recent works start capturing a kinetic aspect of one nucleus of intermetallic compounds.[21,22)] To this end, nucleation and subsequent solidification of alloy system including intermetallic compounds are investigated by large-scale MD simulations in this study. Here, homogeneous nucleation from undercooled melt of Ni–Al alloy is examined. Ni–Al alloy is employed as a model case, in which NiAl has a body center cubic (BCC)-based (B2) structure in spite of both Ni and Al have face centered cubic (FCC) structure. Also, Ni–Al alloy is a good example since it is one of the most practical nickel-base alloy. This paper is organized as follows. After describing the simulation methodology in Section 2, nucleation and solidification from undercooled melt of Ni–50 at%Al is examined in Section 3.1 and those of pure Ni is examined for comparison in Section 3.2. Origin of the polymorphism in stepwise nucleation of Ni and the preferential nucleation of B2-NiAl from melt of Ni–Al alloy is discussed on the basis of classical nucleation theory in Section 4. The conclusions are provided in Section 5.

2. Simulation Methodology

MD simulations are performed using Large-scale Atomic/Molecular Massively Parallel Simulator (LAMMPS).[24)] An embedded atom method (EAM) potential fitted by Purja Pun and Mishin[25)] is employed for the interatomic potential of Ni–Al binary system. The parameter files for the EAM potential listed on the Interatomic Potentials Repository (IPR) at National Institute of Standards and Technology (NIST)[15,16)] are utilized for the MD simulation. The velocity–Verlet method is used to integrate the classical equation of motion with a time step of 1.0 fs. The Nose–Hoover thermostat and barostat[26,27)] are employed to control temperature and pressure. The open visualization tool (OVITO)[28)] is used for visualization of simulation results and post-analyses by adaptive common neighbor analysis (a-CNA)[29)] to identify local atomic structures. The initial configurations for the melt of Ni–50 at%Al and Ni are prepared by heating FCC crystals of Ni and NiAl with 4,000,000 atoms in a cell of 35.2 nm^3 ($100 \times 100 \times 100$ unit cells) at 3000 K for 1 ps with the isobaric-isothermal ensemble. Then, obtained initial

*Corresponding author, E-mail: shibuta@material.t.u-tokyo.ac.jp

structures are relaxed at 1100 K for 3000 ps with the same ensemble and nucleation and subsequent solidification processes are investigated. Periodic boundary condition is employed for all calculations. Note that the melting point of pure Ni of this EAM potential is approximately $T_m = 1680 \pm 20$ K, which is estimated by the convergence temperature technique.[30,31] Detail of this estimation is summarized in Appendix A. After main MD simulations, atomic configurations are analyzed by a-CNA[29] to identify local atomic structures such as FCC, BCC and liquid for all atoms in the simulation cell. Main MD calculations are performed on a high performance computing (HPC) cluster system with Intel(R) Xeon(R) E5-2690 (8 cores/CPU) and 256 cores (32 CPUs) are parallelized with the message passing interface (MPI).

3. Results

3.1 Nucleation and solidification of NiAl from undercooled melt of Ni–50 at% Al

Figure 1(a) shows snapshots of the simulation cell during 3000 ps calculation of nucleation and solidification from undercooled melt of Ni–50 at%Al. Atoms are colored according to local atomic structure defined by a-CNA. Atoms with other configurations by a-CNA (i.e., liquid, grain boundary and other defects) are not shown for the clarity of the figure. It is confirmed from snapshots that multiple events of nucleation happen simultaneously around 200 ps and many of small grains with BCC configuration are subsequently formed. Then, small grains grow into a fine microstructure via solidification by 1000 ps. There is no significant difference in the snapshot after 1000 ps. The structure with BCC configuration defined by a-CNA basically corresponds to B2 structure of NiAl as discussed later. Figure 1(b) shows time dependence of the number of atoms for each local atomic structure defined by a-CNA and that of potential energy per atom in the system. Atoms with BCC configuration drastically increases as soon as multiple nucleation happens and correspondingly the number of atoms with Frank's icosahedral (ICO) and other configurations (i.e., liquid) decreases. Although the number of atoms with FCC and hexagonal close-packed (HCP) configurations slightly increases at the initial stage, these numbers are negligible compared to that of BCC configuration. The potential energy monotonously decreases as nucleation and subsequent solidification proceed. The drop of potential energy becomes the largest at around 750 ps. It corresponds to the drastic increases of atoms with BCC configuration and the decrease of atoms with ICO and other configurations, which represents phase transition from liquid to solid phase.

Figure 2 shows the snapshot of atomic configuration for representative grains obtained after 3000 ps calculation, which is colored by elemental species. The other grains are not shown for the clarity of the figure. As clearly shown in the enlarged view, Ni and Al atoms are arranged alternately. Extracted atoms consist of the sublattice of BCC structure, which is a typical B2 structure (see Fig. 3(a)). This agrees with the knowledge from phase diagram.[32] Then, when does the B2 structure appears? Figure 3(b) shows snapshots of atomic configuration at the initial stage of nucleation from undercooled melt of Ni–50 at%Al. In the snapshots, only

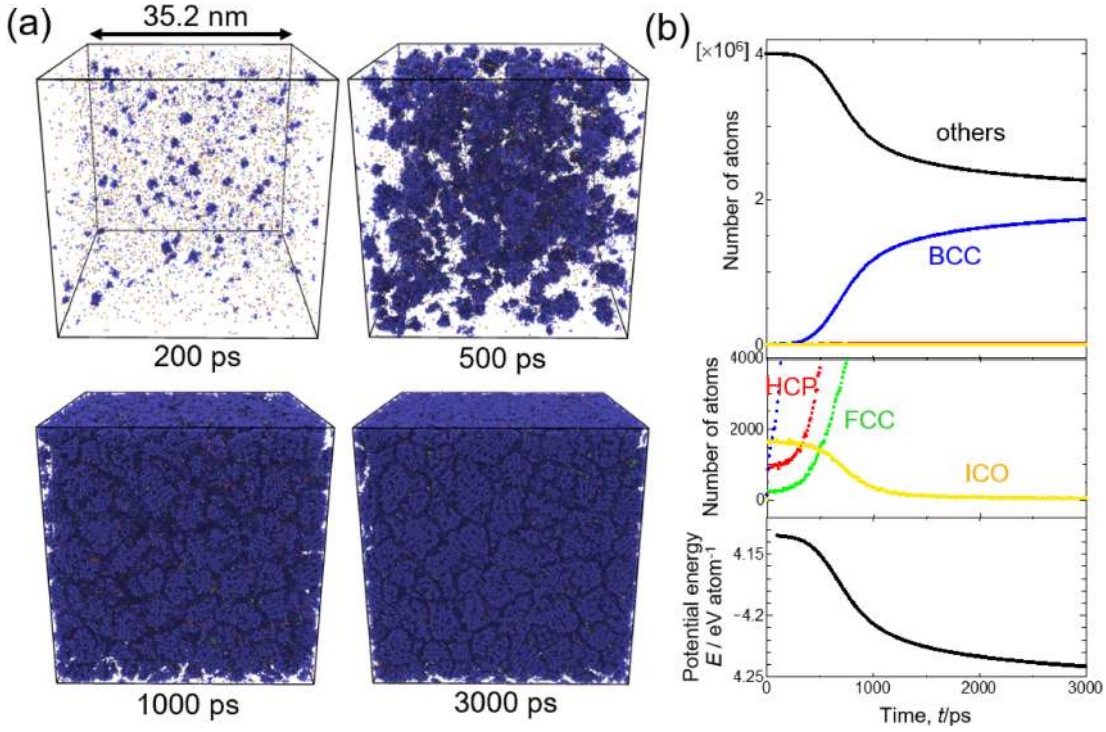

Fig. 1 (a) Snapshots of the simulation cell during 3000 ps calculation of the nucleation and solidification from undercooled melt of Ni–50 at%Al at 1100 K. Blue, red, green yellow atoms represent atoms with BCC, HCP, FCC and Franks' icosahedral (ICO) configurations defined by adaptive common neighbor analysis (a-CNA). Atoms with other configurations (i.e., liquid, grain boundary and other defects) are not shown for the clarity of the figure. (b) Time dependence of the number of atoms for each local atomic structure (top) with an enlarged view around starting point (middle) and the potential energy per atom in the system (bottom).

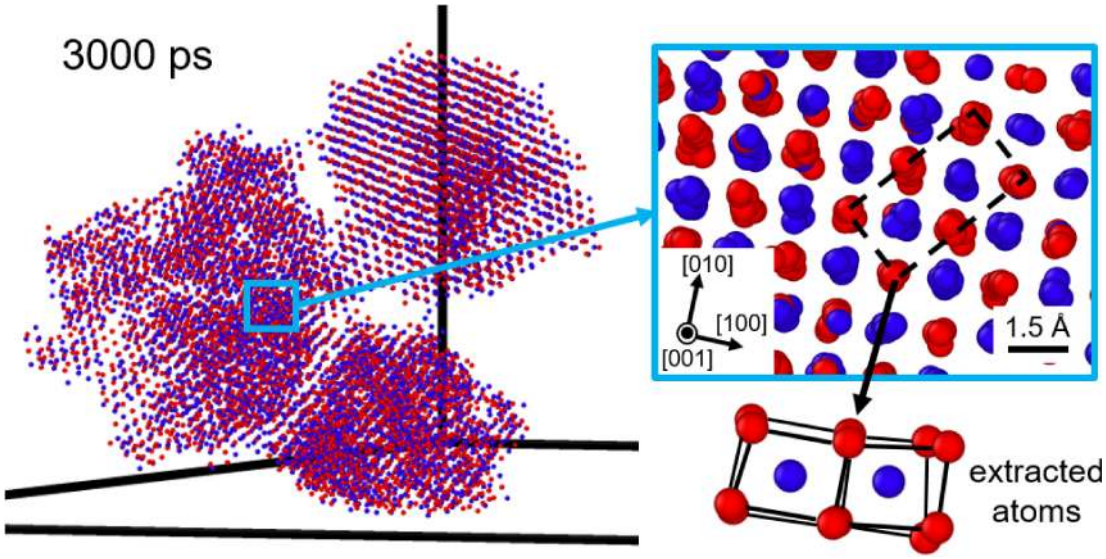

Fig. 2 Snapshots of atomic configuration for representative grains obtained after 3000 ps calculation. Red and blue atoms represent Al and Ni, respectively. Black thick lines represent sides of the calculation cell. The inset shows the enlarged view of atomic configuration of Ni and Al atoms in the grain observed from [001] direction. Structure of atoms extracted from the area shown by black square in the enlarged view is also drawn.

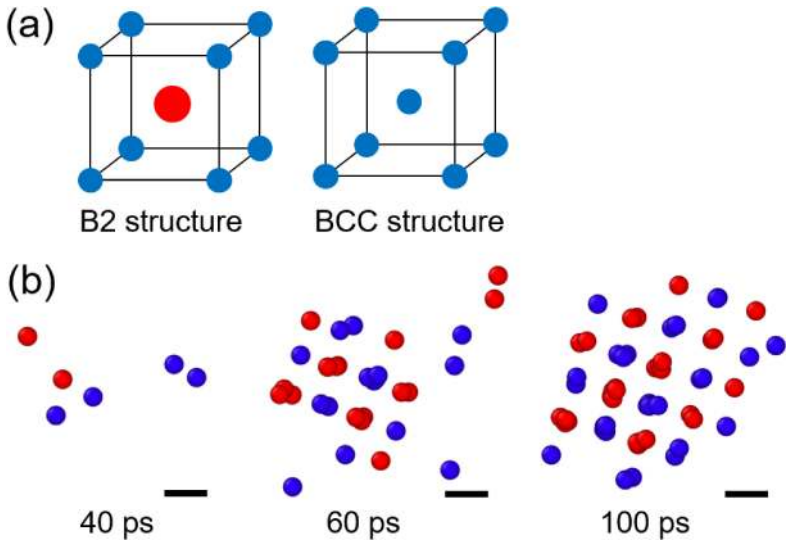

Fig. 3 (a) Crystal structures of B2 and BCC structures. (b) Snapshots of atomic configuration at the initial stage of nucleation from undercooled melt of Ni–50 at%Al. Red and blue atoms represent Al and Ni, respectively. In the snapshots, only atoms with BCC configuration defined by a-CNA are shown. Scale bars represent 1.5 Å.

atoms with BCC configuration defined by a-CNA are shown. Apparently, B2 structure already appears at the very beginning of the nucleation before 100 ps. Therefore, it is considered that the B2 structure of NiAl appears directly via nucleation rather than via preferential nucleation of Ni and (or) Al matrix and subsequent phase transition into B2 phase. The reason of preferential nucleation of B2 structure is quantitatively discussed from kinetic viewpoint in Section 4.

3.2 Nucleation and solidification of pure Ni from undercooled melt

Next, nucleation and solidification from undercooled melt of pure Ni is examined using same interatomic potential for comparison. Figure 4(a) shows snapshots of the simulation cell during 3000 ps calculation of nucleation and solidification from undercooled melt of pure Ni. Atoms are colored according to local atomic structure defined by a-CNA. Atoms with other configurations by a-CNA (i.e., liquid, grain boundary and other defects) are not shown for the clarity of the figure. In the initial stage, atoms with ICO configuration appears in the liquid phase and a BCC nucleus appears among them. Then, the BCC nucleus quickly changes into FCC one and FCC crystal including several stacking faults grows into all parts of the system. Unlike the case of Ni–50 at%Al, only one nucleus grows larger via nucleation from the undercooled melt of pure Ni and an FCC single crystal with several stacking faults is formed as a result.

Figure 4(b) shows time dependence of the number of atoms for each local atomic structure defined by a-CNA and that of potential energy per atom in the system. As observed in the snapshot, the number of atoms with ICO configuration

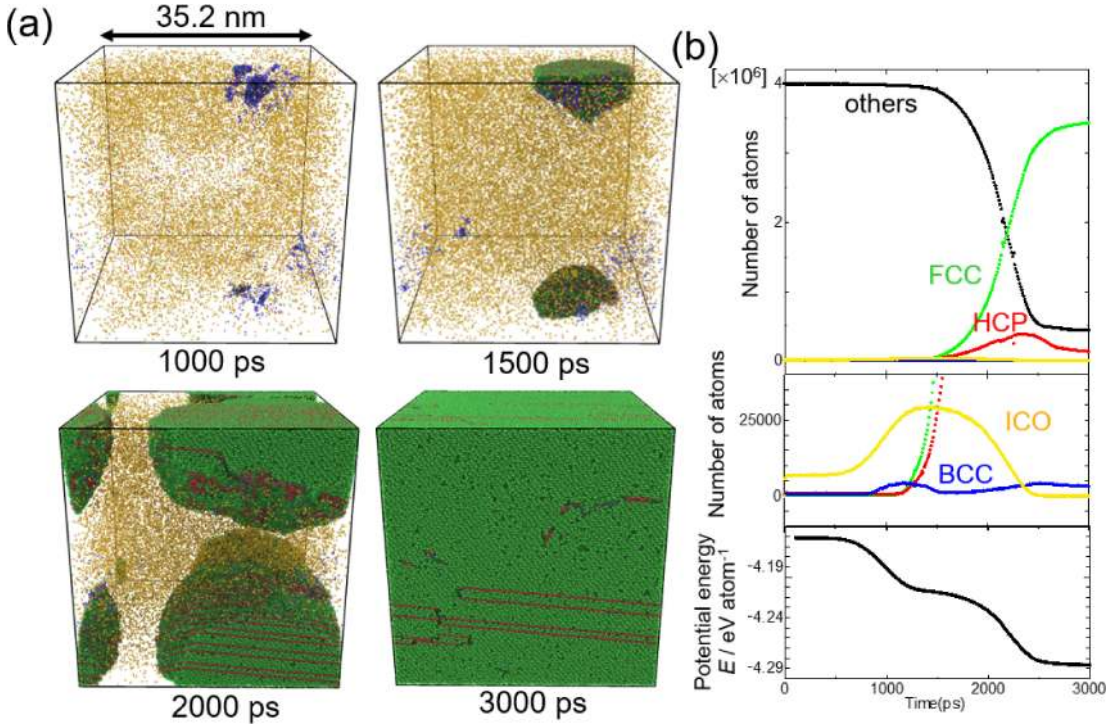

Fig. 4 (a) Snapshots of the simulation cell during 3000 ps calculation of nucleation and solidification from undercooled melt of pure Ni at 1100 K. Blue, green, red and yellow atoms represent atoms with BCC, FCC, HCP and Franks' icosahedral (ICO) configurations defined by a-CNA, respectively. Atoms with other configurations are not shown for the clarity of the figure. (b) Time dependence of the number of atoms for each local atomic structure (top) with an enlarged view around starting point (middle) and the potential energy per atom in the system (bottom).

increases at the beginning, which is followed by the increase of the number of atoms with BCC configuration as shown in the enlarged view. This trend agrees with our previous simulation of homogeneous nucleation of BCC-Fe from undercooled melt iron,[11] in which the local accumulation of atoms with the ICO configuration in the undercooled melt enhanced the nucleation of BCC-Fe nuclei. Then, the number of atoms with FCC configuration drastically increases while those of ICO and BCC configuration decreases. As the number of atoms with FCC configuration increases, that of HCP configuration slightly increases. However, this represents the formation of stacking faults in FCC rather than that of HCP phase as shown in the snapshot. Note that CNA technique does not distinguish between stacking fault in FCC and bulk HCP structure in general. Interestingly, potential energy as a function of time drops in two steps. That is, first drop happens when the number of atoms with ICO and subsequent BCC configuration increases. After a short plateau stage, second drop happens when the number of atoms with FCC configuration increases. Since BCC phase is metastable and FCC phase is stable for pure Ni, it is considered that stepwise phase transition happens, which leads to polymorphism during the nucleation stage.

Nucleation of metastable phase from undercooled melt under large undercooling temperature has long been known as Ostwald's step rule[33] and it has been widely observed in experiments over many years.[34–37] According the Ostwald's step rule, free energy hierarchy, which is relative magnitude of driving forces among the possible phase transitions, causes stepwise phase transition via metastable phases. The stepwise phase transition has been widely discussed from thermodynamic viewpoint[36] and these discussions have contributed the interpretation of rapid cooling technique from practical viewpoint.[37] On the other hand, polymorphism during nucleation has been also found in recent MD simulations.[6,7,38] In these studies, BCC-like nucleus first appeared and transformed into FCC crystals from inner of the preordered cluster even though the Lennard-Jones potential was employed, in which FCC structure should be stable. Figure 5 shows snapshots of stepwise phase transition during the nucleation from undercooled melt of pure Ni observed in Fig. 4. A BCC nucleus appears from undercooled melt and it transforms into FCC one from inner of the cluster, which agrees with previous reports by MD simulations.[6,7] Therefore, it is considered that the stepwise phase transition occurs via polymorphism within nucleus rather than mere competition between BCC and FCC nucleation from undercooled melt.

4. Discussion

Here, polymorphism in a small nucleus is discussed from kinetic viewpoint. According to classical nucleation theory,[2] nucleation of spherical nucleus with radius r in the undercooled melt cause a difference in free energy as:

$$\Delta G = 4\pi r^2 \sigma_{SL} - \frac{4}{3}\pi r^3 \Delta G_V \quad (1)$$

where ΔG_V is the difference in Gibbs free energy between liquid and solid, and σ_{SL} is the solid-liquid interfacial energy. Now, let us consider eq. (1) for following three cases: (i) BCC nucleation from undercooled melt, (ii) FCC nucleation

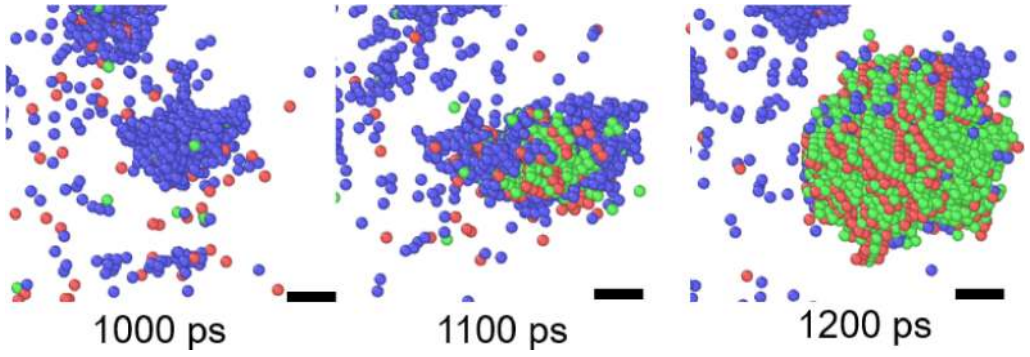

Fig. 5 Snapshots of stepwise phase transition during the nucleation from undercooled melt of pure Ni. Scale bars represent 0.5 nm. Blue, green and red atoms represent atoms with BCC, FCC and HCP configurations defined by a-CNA, respectively. Atoms with other configurations are not shown for the clarity of the figure.

from undercooled melt, and (iii) FCC nucleation from BCC crystal. To discuss our MD results quantitatively, ΔG_V and σ_{SL} for above three cases should be derived using the EAM potential employed in this study.[25] ΔG_V can be derived using the following Gibbs-Helmholtz equation relation:[39]

$$\left[\frac{\partial}{\partial T}\left(\frac{\Delta G_V}{T}\right)\right]_P = -\frac{\Delta H_V}{T^2} \quad (2)$$

where ΔH_V ($= H_L - H_S$) is the difference in enthalpy, H between liquid (L) and solid (S) and T is the temperature. Since ΔG_V becomes zero at the melting point T_m, following relation is obtained.

$$\Delta G_V(T) = T\int_T^{T_m} \frac{\Delta H_V(T')}{T'^2}\,dT' \quad (3)$$

Since the enthalpy can be directly calculated from MD simulation, ΔG_V can be derived from the difference in enthalpy between solid and liquid.[39] Assuming temperature dependence of enthalpy to be linear as $H = aT + b$ (a, b: constant), eq. (3) can be summarized as

$$\Delta G_V(T) = (a_L - a_S)T\log\frac{T_m}{T} + (b_L - b_S)\left(1 - \frac{T}{T_m}\right) \quad (4)$$

Thus, ΔG_V is derived using parameters, a_L, a_S, b_L and b_S. Figure 6(a) shows temperature dependence of enthalpy of liquid, FCC crystal and BCC crystal of pure Ni calculated using the EAM potential employed in main MD simulations. Systems with 32000 ($20 \times 20 \times 20$ unit cells), 4000 ($10 \times 10 \times 10$ unit cells), and 16 atoms ($2 \times 2 \times 2$ unit cells) are employed for liquid, FCC and BCC phase. Note that a small system is employed for BCC Ni to utilize constraint of structure by periodic boundary condition since BCC crystal of Ni is not stable basically. From fitting lines in Fig. 6(a), parameters a and b are estimated to be $a_L = 4.04 \times 10^{-4}$, $b_L = -4.46$, $a_{S(FCC)} = 2.83 \times 10^{-4}$, $b_{S(FCC)} = -4.45$, $a_{S(BCC)} = 2.57 \times 10^{-4}$ and $b_{S(FCC)} = -4.41$, respectively. Substituting these values in eq. (4), temperature dependence of the difference in Gibbs free energy between liquid and BCC, liquid and FCC, and BCC and FCC around 1100 K is derived as shown in Fig. 6(b). ΔG_V between liquid and FCC phase is approximately 2.5 times larger than that between liquid and BCC phase at 1100 K.

On the other hand, it is not straightforward to estimate solid-liquid interfacial energy for the BCC-liquid interface

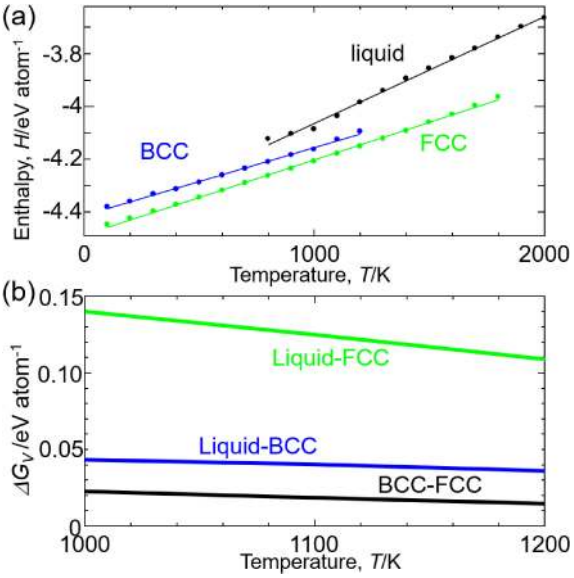

Fig. 6 Temperature dependence of (a) enthalpy of liquid, FCC crystal and BCC crystal and (b) the difference in Gibbs free energy between liquid and FCC, liquid and BCC, and BCC and FCC for pure Ni by the EAM potential employed in main MD simulations.

since BCC phase does not exist stable at high temperature. Therefore, we employed the Turnbull's equation,[40] $\sigma_{SL} = \alpha\Delta H_V\rho^{2/3}$, where ρ is the number density of crystal and α is the Turnbull's coefficient. Here, $\alpha_{FCC} = 0.55$ and $\alpha_{BCC} = 0.29$ are employed, which are derived by fitting solid-liquid interfacial energies of various metals from MD simulations.[41] $\rho_{FCC} = 91.71\,\mathrm{atom/nm^3}$ and $\rho_{BCC} = 84.28\,\mathrm{atom/nm^3}$ are employed, which are directly derived from MD simulations in Fig. 6(a) at 1100 K. Using values of ΔH_V in Fig. 6(a), $\sigma_{SL(FCC)}$ and $\sigma_{SL(BCC)}$ are estimated to be 320 and 148 $\mathrm{mJ/m^2}$, respectively. Most of the previously reported values of $\sigma_{SL(FCC)}$ for pure Ni are within the range between 250 and 350 $\mathrm{mJ/m^2}$.[40,42,43] Therefore, solid-liquid interfacial energy estimated from our MD results are considered to be reasonable. Moreover, grain boundary energy of BCC-FCC hetero-interface, $\sigma_{BCC/FCC}$ is calculated from the difference between the energy of a BCC-FCC bicrystal and the total energy of the constituent crystals.[31] Here, we employ a BCC-FCC hetero-interface with Nishiyama-Wassermann (N-W) relation[44] known as $(110)_{BCC}//(111)_{FCC}$ and $[001]_{BCC}//$

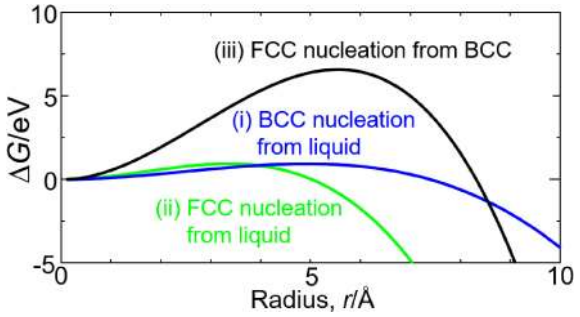

Fig. 7 Difference in free energy as a function of nucleus size for (i) BCC nucleation from undercooled melt (blue curve), (ii) FCC nucleation from undercooled melt (green curve) and (iii) FCC nucleation from BCC crystal (black curve) at 1100 K.

$[1\bar{1}0]_{FCC}$. The N-W relation is employed as one of the representative semi-coherent interfaces of BCC-FCC hetero-interface, which fits with a rectangle cell with periodic boundary condition. The size of constituent crystals is $484.8 \times 77.49 \times 28.7$ Å^3 with 129600 atoms for BCC crystal and $484.8 \times 77.49 \times 35.2$ Å^3 with 210180 atoms for FCC crystal, respectively. $\sigma_{BCC/FCC}$ is estimated to be 821 mJ/m^2. Note that $\sigma_{BCC/FCC}$ depends on the orientation relationship between BCC and FCC crystals and therefore the value of $\sigma_{BCC/FCC}$ employed here is a reference value as a first approximation.

Figure 7 shows ΔG as a function of nucleus size at 1100 K for (i) BCC nucleation from undercooled melt, (ii) FCC nucleation from undercooled melt and (iii) FCC nucleation from BCC crystal, which are defined by eq. (1) with parameters derived above. Comparing case (i) and (ii), ΔG for BCC nucleation from undercooled melt is lower than that of the FCC nucleation for nucleus of radius smaller than 4 Å. Therefore, it is reasonable that BCC nucleus first appears in the undercooled melt in the MD simulation. This is due to the effect of lower solid-liquid interfacial energy of BCC-liquid interface than that of FCC-liquid interface. However, the difference in ΔG of BCC and FCC nucleation from liquid is not so significant, which does not exclude the possibility of direct FCC nucleation from the undercooled melt. After these two lines cross around 4 Å and ΔG of FCC nucleation from liquid becomes lower than that of BCC case at larger radius than 4 Å. However, it does not mean instantaneous phase transformation from BCC to FCC phase since these two lines represent for ΔG of BCC and FCC nucleation from liquid phase. Rather, it is important to compare cases (i) and (iii). That is, ΔG for FCC nucleation from BCC matrix becomes lower than that for BCC nucleation from undercooled melt at larger than 9 Å, where these two lines are crossing. That is, FCC nucleation can occur from the inside of previously existing BCC nucleus with a radius of approximately 1 nm or larger since the emergence of FCC from BCC phase is energetically favorable compare to further growth of BCC phase. Actually, the radius in short-axis direction of the elliptical nucleus at 1100 ps in Fig. 5 is about 1.2–1.3 nm. Therefore, above discussion well explains the polymorphism in nucleation found in our simulation.

Next, preferential nucleation of B2 structure of NiAl from undercooled melt of Ni–50 at%Al is discussed from kinetic viewpoint in the same manner as above discussion on the

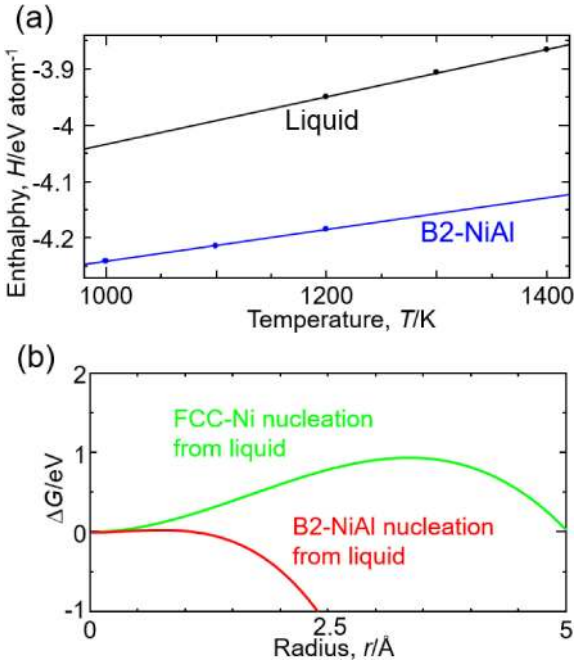

Fig. 8 (a) Temperature dependence of enthalpy of liquid alloy of Ni–50 at%Al and B2-NiAl crystal. (b) Difference in free energy as a function of nucleus size for B2-NiAl nucleation from undercooled melt of Ni–50 at%Al (red curve) at 1100 K. For comparison, FCC-Ni nucleation from undercooled melt of pure Ni (green curve) at 1100 K in Fig. 7 is drawn.

polymorphism. Figure 8(a) shows temperature dependence of enthalpy of the melt of Ni–50 at%Al and the B2-NiAl crystal around 1100 K using the EAM potential employed in main MD simulations. Systems with 1000 Ni and 1000 Al atoms ($10 \times 10 \times 10$ unit cells of B2 structure) are employed for both cases. From fitting lines in Fig. 8(a), parameters a and b in eq. (4) are estimated to be $a_L = 4.20 \times 10^{-4}$, $b_L = -4.45$, $a_{S(B2)} = 2.83 \times 10^{-4}$ and $b_{S(B2)} = -4.52$, respectively. The melting point of B2-NiAl crystal of the EAM potential employed in this study is 1780 ± 20 K by the convergence temperature technique.[30,31] Substituting these values in eq. (4), the difference in Gibbs free energy between Ni–50 at%Al melt and B2-NiAl (ΔG_V) at 1100 K is estimated to be 9.93×10^{-2} eV/atom. Number density of B2-NiAl crystal (ρ_{B2_NiAl}) at 1100 K is estimated to be 83.7 atom/nm^3 from the MD simulation in Fig. 8(a) at 1100 K. The solid-liquid interfacial energy of the B2(NiAl)-liquid (Ni–50 at%Al) interface, $\sigma_{SL(B2\text{-}NiAl)}$ is estimated to be 195 mJ/m^2 from the Turnbull's equation with values $\alpha_{BCC} = 0.29$ and ΔH_V estimated from Fig. 8(a).

Figure 8(b) shows ΔG as a function of nucleus size for B2-NiAl nucleation from undercooled melt of Ni–50 at%Al at 1100 K. For comparison, ΔG for FCC-Ni nucleation from undercooled melt of pure Ni at 1100 K in Fig. 7 is drawn. Note that ΔG for FCC-Ni nucleation from undercooled melt of pure Ni is employed for comparison since there is no significant difference in the solid-liquid interfacial energy of NiAl-liquid interface for the case of melt of pure Ni and that of Ni–50 at%Al as far as assuming the Turnbull's relation.[40] It is confirmed that ΔG for B2-NiAl nucleation from undercooled melt of Ni–50 at%Al is much lower than that of the FCC-Ni nucleation at any nucleus size. This is because $\sigma_{SL(B2\text{-}NiAl)}$ is smaller than $\sigma_{SL(FCC)}$ and ΔG_V between Ni–

50 at%Al melt and B2-NiAl is larger than that between liquid and FCC-Ni. Larger ΔG_V for B2-NiAl than that of FCC Ni is mainly caused by larger cohesive energy of B2-NiAl crystal (−4.51 eV/atom[25]) compared to that of FCC-Ni (−4.45 eV/atom[25]). It is considered that this trend is applicable for the case of FCC-Al nucleation since solid-liquid interfacial energy of FCC-based crystal is basically larger than that of BCC-based crystal according to the Turnbull's relation.[40] Therefore, it is reasonable that the B2 structure of NiAl appears directly via nucleation rather than via preferential nucleation of matrix phase in our MD simulation. Moreover, low energy barrier for the nucleation of B2-NiAl well explains the nucleation of B2-NiAl from an early stage (i.e., almost no incubation time), whereas the nucleation of pure Ni has a long incubation time of approximately 1000 ps at the same temperature.

5. Conclusions

In this study, nucleation from undercooled melt of Ni–Al alloy is investigated by MD simulation. NiAl nuclei with B2 structure directly appears from the undercooled melt of Ni–50 at%Al. On the other hand, stepwise phase transition happens in the nucleation from undercooled melt of pure Ni. That is, FCC nucleation occurs from the inside of previously existing BCC nucleus. The origin of such polymorphism is discussed on the basis of the classical nucleation theory. Emergence of FCC from BCC phase is energetically favorable compare to further growth of BCC phase at a certain size of nucleus. Moreover, the preferential nucleation of B2-NiAl from undercooled melt of Ni–50 at%Al is well explained by the classical nucleation theory. In conclusion, it is significant in this study to shed light on a kinetic aspect of polymorphism in nucleation from atomistic viewpoint since it is not straightforward to discuss it only from the observation from experimental approach. Moreover, it is encouraging us from viewpoint of computational metallurgy that various types of nucleation can be explained using one consistent interatomic potential universally. The concentration dependence of nucleation for various practical alloys will be studied in the next step.

Acknowledgments

This work was supported by Grant-in-Aid for Scientific Research (B) [Nos. 16H04490, 19H02415] from Japan Society for the Promotion of Science (JSPS), Japan.

Appendix A. Estimation of melting point by converging temperature technique.

Melting point in MD simulation using an interatomic potential tends to deviate from the experimental value mainly due to the difficulty of directly reading the melting point from the interatomic potential curve itself.[31] Therefore, the melting point defined by the interatomic potential should be known in advance of main MD simulation. The melting point of pure metal is estimated from equilibrium temperature of a solid-liquid biphasic system, where the planar solid-liquid interface does not move.[31] Figure A1 shows time dependence of the temperature of a solid-liquid biphasic Ni system with 96,000 atoms in a cell of 70.4 × 70.4 × 311.2 Å calculated by the EAM potential employed in main MD simulation.[25] The biphasic system is first relaxed with the isobaric–isothermal ensemble for 50 ps at 1600, 1670, and 1800 K. Then, the system is relaxed with the isenthalpic–isobaric ensemble for 950 ps. Temperatures converge to approximately 1680 ± 20 K, which is regarded as the melting point of Ni expressed by this EAM potential.

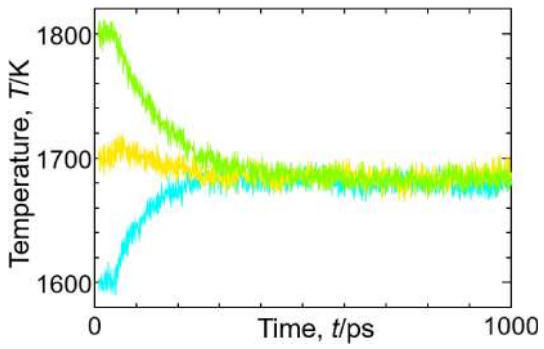

Fig. A1 Time dependence of temperature of a solid-liquid biphasic Ni system calculated by the EAM potential employed in main MD simulation.

REFERENCES

1) A. Onuki: *Phase Transformation Dynamics*, (Cambridge University Press, Cambridge, 2002) pp. 488–551.
2) J.A. Dantzig and M. Rappaz: *Solidification*, (EPFL Press, Lausanne, 2009) pp. 249–285.
3) G.C. Sosso, J. Chen, S.J. Cox, M. Fitzner, P. Pedevilla, A. Zen and A. Michaelides: Chem. Rev. **116** (2016) 7078–7116.
4) S. Auer and D. Frenkel: Nature **409** (2001) 1020–1023.
5) R.S. Aga, J.R. Morris, J.J. Hoyt and M. Mendelev: Phys. Rev. Lett. **96** (2006) 245701.
6) P.R. ten Wolde, M.J. Ruiz-Montero and D. Frenkel: Phys. Rev. Lett. **75** (1995) 2714–2717.
7) C. Desgranges and J. Delhommelle: J. Am. Chem. Soc. **128** (2006) 10368–10369.
8) F.J. Cherne, M.I. Baskes, R.B. Schwarz, S.G. Srinivasan and W. Klein: Model. Simul. Mater. Sci. Eng. **12** (2004) 1063–1068.
9) G. Díaz Leines, R. Drautz and J. Rogal: J. Chem. Phys. **146** (2017) 154702.
10) T. Fujinaga and Y. Shibuta: Comput. Mater. Sci. **164** (2019) 74–81.
11) Y. Shibuta, S. Sakane, E. Miyoshi, S. Okita, T. Takaki and M. Ohno: Nat. Commun. **8** (2017) 10.
12) Y. Shibuta, S. Sakane, E. Miyoshi, T. Takaki and M. Ohno: Model. Simul. Mater. Sci. Eng. **27** (2019) 054002.
13) Y. Shibuta, M. Ohno and T. Takaki: JOM **67** (2015) 1793–1804.
14) Y. Shibuta, M. Ohno and T. Takaki: Adv. Theory Simul. **1** (2018) 1800065.
15) NIST Interatomic potentials repository: DOI: 10.18434/m37.
16) C.A. Becker, F. Tavazza, Z.T. Trautt and R.A. Buarque de Macedoc: Curr. Opin. Solid State Mater. Sci. **17** (2013) 277–283.
17) E.B. Tadmor, R.S. Elliott, J.P. Sethna, R.E. Miller and C.A. Becker: JOM **63**(7) (2011) 17.
18) K.D. Watson, S.E.T. Nguelo, C. Desgranges and J. Delhommelle: CrystEngComm **13** (2011) 1132–1140.
19) W.-S. Ko, S.B. Maisel, B. Grabowski, J.B. Jeon and J. Neugebauer: Acta Mater. **123** (2017) 90–101.
20) H. Lin, T. Li and H. Li: Phys. Chem. Chem. Phys. **20** (2018) 29856–29865.
21) H. Song, Y. Sun, F. Zhang, C.Z. Wang, K.M. Ho and M.I. Mendelev: Phys. Rev. Mater. **2** (2018) 023401.

22) Y. Sun, F. Zhang, H. Song, M.I. Mendelev, C.-Z. Wang and K.-M. Ho: J. Phys. Chem. C **123** (2019) 6685–6692.
23) Y. Cui, H. Chen, G. Yang, L. Ye, B. Liu, D. Gao, H. Luo and Y. Gao: J. Alloy. Compd. **740** (2018) 863–869.
24) S.J. Plimpton: J. Comput. Phys. **117** (1995) 1–19.
25) G.P. Purja Pun and Y. Mishin: Philos. Mag. **89** (2009) 3245–3267.
26) S. Nosé: J. Chem. Phys. **81** (1984) 511–519.
27) W.G. Hoover: Phys. Rev. A **31** (1985) 1695–1697.
28) A. Stukowski: Model. Simul. Mater. Sci. Eng. **18** (2010) 015012.
29) A. Stukowski: Model. Simul. Mater. Sci. Eng. **20** (2012) 045021.
30) Y. Shibuta, S. Takamoto and T. Suzuki: ISIJ Int. **48** (2008) 1582–1591.
31) Y. Shibuta: Mater. Trans. **60** (2019) 180–188.
32) T.B. Massalski, H. Okamoto, P.R. Subramanian and L. Kacprzak (eds.): *Binary Alloy Phase Diagrams*, 2nd ed., (ASM International, International Materials Park, OH, 1990) pp. 140–144.
33) W. Ostwald: Z. Phys. Chem. **22** (1897) 289–330.
34) G. Tammann: *Aggregatzustände*, (Verlag Von Leopold Voss, Leipzig, 1922) p. 234.
35) J.C. Baker and J. Cahn: *Solidification*, (ASM International, International Materials Park, OH, 1971) p. 23.
36) K.N. Ishihara, M. Maeda and P.H. Shingu: Acta Metall. **33** (1985) 2113–2117.
37) H. Shingu and K. Ishihara: Bull. JIM **25** (1986) 16–23.
38) H. Wang, H. Gould and W. Klein: Phys. Rev. E **76** (2007) 031604.
39) C.A. Becker, M. Asta, J.J. Hoyt and S.M. Foiles: J. Chem. Phys. **124** (2006) 164708.
40) D. Turnbull: J. Appl. Phys. **21** (1950) 1022–1028.
41) J.J. Hoyt, M. Asta, T. Haxhimali, A. Karma, R.E. Napolitano, R. Trivedi, B.B. Laird and J.R. Morris: MRS Bull. **29** (2004) 935–939.
42) Y. Waseda and W.A. Miller: Trans. JIM **19** (1978) 546–552.
43) B. Vinet, L. Magnusson, H. Fredriksson and P.J. Desré: J. Colloid Interface Sci. **255** (2002) 363–374.
44) S. Tateyama, Y. Shibuta and T. Suzuki: Scr. Mater. **59** (2008) 971–974.